Journal of Magnetism and Magnetic Materials 579 (2023) 170853

Contents lists available at ScienceDirect

Journal of Magnetism and Magnetic Materials

journal homepage: www.elsevier.com/locate/jmmm

Research article

Structural, magnetic and electronic properties of L2$_1$-ordered $Ru_{2-x}Mn_{1+x}Al$ Heusler alloy thin films

K.E. Siewierska [a], H. Kurt [b], B. Shortall [a], A. Jha [a], N. Teichert [a], G. Atcheson [a], M. Venkatesan [a], J.M.D. Coey [a], Z. Gercsi [a], K. Rode [a,*]

[a] School of Physics and CRANN, Trinity College Dublin, Ireland
[b] Istanbul Medeniyet University, Department of Engineering Physics, Goztepe Istanbul 34700, Turkey

ARTICLE INFO

Keywords:
Heusler alloy
Spin polarisation
Magnetotransport
Thin films

ABSTRACT

The cubic Heusler alloy $Ru_{2-x}Mn_{1+x}Al$ is grown in thin film form on MgO and $MgAl_2O_4$ substrates. It is a highly spin-polarised ferrimagnetic metal, with weak magnetocrystalline anisotropy. Although structurally and chemically similar to Mn_2Ru_xGa, it does not exhibit ferrimagnetic compensation, or large magneto galvanic effects. The differences are attributed to a combination of atomic order and the hybridisation with the group 13 element Al or Ga. The spin polarisation is around 50% to 60%. There is a gap in the density of states just above the Fermi level in fully ordered compounds.

1. Introduction

Antiferromagnetic spin electronics is attracting considerable interest due to the relative abundance of antiferromagnetically coupled materials, the fast magnetisation dynamics and the insensitivity to external magnetic fields along with the absence of demagnetising forces. A major difficulty is control and read-out of the antiferromagnetic state. A compensated ferrimagnet where two antiferromagnetically coupled, but inequivalent, sublattices produce zero net moment at the compensation temperature T_{comp} potentially combines the advantages of antiferromagnets, [1,2] with those of a ferromagnetic metal. The magnetisation can be controlled by an external field away from T_{comp}, coupled with a high transport spin polarisation that facilitates reading the magnetic state using magneto-optical Kerr effect [3–5], anomalous Hall effect (AHE), [6] and giant- or tunnel-magnetoresistance [7] (GMR or TMR).

In 1995, van Leuken and de Groot [8] proposed that some half-Heusler alloys ($C1_b$ structure) would exhibit magnetic compensation, yet due to the inequivalent magnetic sublattices exhibit 100% spin polarisation and thus be half metallic. Subsequent work followed the empirical Slater-Pauling rule, [9] $M = N_v - 18$ for half-Heuslers and $M = N_v - 24$ for full Heuslers. N_v is the number of valence electrons, M the magnetisation in μ_B per formula unit (μ_B f.u.$^{-1}$). The $D0_3$ phase of Mn_3Ga and Mn_3Al were suggested as possible compensated half-metallic ferrimagnets, [10] but neither crystallise in the $D0_3$ structure in the bulk. There is a report on the growth of $D0_3$-structure Mn_3Al thin films on GaAs substrates with a net moment of 0.017 μ_B f.u.$^{-1}$ and a Curie temperature of 605 K [11]. Disordered antiferromagnetic Mn_3Al films with a cubic structure and a Neél temperature of 400 K were also grown on MgO substrates [12]. The equilibrium phase for Mn_2Ga and Mn_3Ga is hexagonal $D0_{19}$ which can be changed to tetragonal $D0_{22}$ by annealing at 400 °C [13]. On the other hand Mn_2Al and Mn_3Al crystallise in the cubic β-Mn structure and do not order magnetically but are spin glasses [14]. The materials can also be grown in the $D0_{19}$ hexagonal structure when they are produced as epitaxial sputtered films on suitable seed layers [15].

The first experimental example of a compensated half metallic ferrimagnet, was MRG, the near-cubic Mn-Ru-Ga alloy with formula Mn_2Ru_xGa, discovered by Kurt et al. [16] in 2014. MRG crystallises in space group $F\bar{4}3m$ (XA). The Ru concentration x allows tuning of T_{comp} and also helps to stabilise the near-cubic structure. The original composition with $x = 0.5$ was initially thought to have $N_v = 21$ valence electrons and a half-filled Ru sublattice, but a recent study [17] established that the films contained few vacant sites and $N_v \approx 24$. Compensated ferrimagnetism has also been demonstrated in bulk $Mn_{1.5}FeV_{0.5}Al$, a quaternary Heusler alloys with 24 valence electrons [18,19]. Half-metallic compensated ferrimagnetic materials, such as MRG, are of interest for spin orbit torque switching [20,21] as well as magnetic oscillations in the terahertz region for high-speed, [22,23] on-chip communications [24,25].

The magnetic and transport properties of MRG including their dependence on the Ru content x are understood in a rigid band model.

* Corresponding author.
E-mail addresses: siewierk@tcd.ie (K.E. Siewierska), rodek@tcd.ie (K. Rode).

https://doi.org/10.1016/j.jmmm.2023.170853
Received 10 February 2023; Received in revised form 12 May 2023; Accepted 17 May 2023
Available online 23 May 2023

One sublattice (formed by states originating from Mn in Wyckoff position 4*c*) dominates the band structure around the Fermi level and is coupled antiferromagnetically to another (formed by Mn in position 4*a*) whose states are sufficiently deep to not contribute significantly to the transport. In this model, the role of Ru is to contribute extra electrons to the 4*c* sublattice and hence increase its moment and thus T_{comp}. The role of the group 13 element, Ga, is ignored. Albeit simplistic, this model explains most of the properties of MRG. Its experimental validation was provided by Siewierska et al. [17] who found an excellent linear relation between the number of valence electrons and magnetisation — one added valence electron increases the magnetisation by one μ_B per formula unit.

Here we change from Ga to Al to produce thin films of MRA, the Mn-Ru-Al Heusler alloy whose formula is best written $Ru_{2-x}Mn_{1+x}Al$, and report optimised growth conditions, structural and magnetic properties along with magnetotransport and spin polarisation measurements for films crystallising in space group $Fm\bar{3}m$ ($L2_1$ structure) with Al and Mn in the 4*a*–4*b* plane and Ru occupying the 8*c* central cube. When $x > 0$, excess Mn occupies a fraction of the 8*c* positions, now split into 4*c* and 4*d*. Note that $4a, c$ and $4b, d$ are symmetrically equivalent. The comparison of the two compounds illustrates the importance of crystalline order in this group of Heusler alloys and highlights the role of Ga.

2. Methodology

Epitaxial thin films of MRA were grown by DC magnetron sputtering, using our Shamrock sputtering system, on 10 mm × 10 mm (100) $SrTiO_3$ (STO), $MgAl_2O_4$ (MAO) and MgO substrates. Samples were co-sputtered in argon from a Mn_2Al target (from Kojundo Chemical Laboratory Co. Ltd, Japan) and a Ru target in a confocal sputtering geometry onto the substrates maintained at an optimised deposition temperature (T_{dep}) we found to be 425 °C. Prior to deposition, the back of the substrates was coated with Ti or Ta to ensure uniform absorption of heat and keep T_{dep} constant during deposition. The films had an average thickness of 60 nm and were capped *in-vacuo* with a 2 nm layer of AlO_x deposited at room temperature in order to prevent oxidation. We note that this arrangement of targets does not yield perfect $Ru_{2-x}Mn_{1+x}Al$ stoichiometry as a decrease in Mn also leads to decreased Al content. The sum of the amounts of Ru and Mn in the formula unit varies from 3.0 to 3.3 in our samples, and we therefore write the formula as $Ru_{2-x}Mn_{1+x}Al$ where it is implicit that Al is sub-stoichiometric by up to 30 %.

A Bruker D8 Discover X-ray diffractometer with a copper Kα X-rays and a double-bounce Ge [220] monochromator (λ = 154.06 pm) was used to determine the diffraction patterns and reciprocal space maps (RSM) of the thin films. The substrate (113) reflection is in the same plane as the MRA (204) reflection and it was used to calculate the lattice parameters. Low angle X-ray reflectivity and symmetric X-ray diffraction patterns were measured using a Panalytical X'Pert Pro (λ = 154.19 pm) diffractometer. Film thickness and density were found by fitting the interference pattern using X'Pert Reflectivity software. The compositions were determined from the observed X-ray density inferred from the fit of the low-angle X-ray reflectivity. Using the lattice parameters obtained by reciprocal space mapping and assuming full occupancy of the unit cell, we calculate x for each sample. In our previous work, [17] we found that the densities predicted using this methodology agree to within 1% of the experimental value.

Low-field anomalous Hall effect (AHE) measurements were performed in a 1 T GMW electromagnet system in ambient conditions. Silver wires were cold-welded to the thin films with indium and the current used was 5 mA. Higher field measurements were performed in a superconducting magnet which had a maximum field of 4 T with a cryostat for low-temperature magneto-transport. The films were contacted with silver paint. The 4-point Van der Pauw geometry was used to determine both the Hall and the longitudinal resistivity of the films.

Point contact Andreev reflection (PCAR) measurements were also performed in a Quantum Design PPMS using a mechanically-sharpened Nb tip. The landing of tip onto the sample surface is carefully controlled by an automated vertical attocube™ piezo stepper. Two horizontal steppers are used to move the sample laterally to probe a pristine area. The differential conductance spectra were fitted using a modified Blonder-Tinkham-Klapwijk model, as detailed elsewhere [26,27].

Measurements of the magnetisation with a magnetic field applied perpendicular or parallel to the surface of the films were carried out using a 5 T Quantum Design SQUID magnetometer. These data were corrected for the diamagnetism of the substrate by linear subtraction.

Ab-initio calculations based on density functional theory (DFT) were carried out using norm-conserving pseudopotentials and pseudo-atomic localised basis functions implemented in the OpenMX software package [28]. The generalised gradient approximation (GGA-PBE) approach was used for all calculations. The structure was fully relaxed to minimise interatomic forces. We used a 16-atom supercell with $17 \times 17 \times 17$ k-points to evaluate the total energies. Pre-generated pseudopotentials and pseudo-atomic orbitals with a cut-off radius of 6, 7 and 7 atomic units (a.u.) were used for Mn, Ru and Al elements, respectively. An energy cut-off of 300 Ry was used for numerical integrations. The convergence criterion for the energy minimisation procedure was set to 1×10^{-8} Hartree. The spin orbit interaction (SOI) was turned off for the calculations.

3. Results & discussion

3.1. Structure

We first determine a suitable substrate for the growth of $Ru_{2-x}Mn_{1+x}Al$ thin films, and optimise the deposition temperature T_{dep}. MRG has a lattice parameter of $a_0 \approx 600$ pm and its epitaxial relation with the MgO substrate ensures that the in-plane [100] direction of MgO is parallel to the [110] direction of MRG, $a_{MRG} \approx \sqrt{2}a_{MgO} = 595.6$ pm. We therefore explore the growth of MRA on MgO, $SrTiO_3$ (STO, $\sqrt{2}a$ = 552.3 pm) and $MgAl_2O_4$ (MAO, $\sqrt{2}a$ = 571.8 pm).

In Fig. 1(a) (left column) we show X-ray diffraction patterns of $Ru_{1.9}Mn_{1.1}Al$ on MgO, MAO and STO. MRA does not crystallise on STO, while on both MAO and MgO the films are fully textured with the growth axis parallel to the [001] crystal direction. There are only minor differences between MgO and MAO, and we select MgO as the preferred substrate. In Fig. 1(a) (right column) the deposition temperature T_{dep} is varied from 350 °C to 440 °C. Although a minor secondary phase is present in all samples, it is nearly suppressed at T_{dep} = 425 °C. Finally, in Fig. 1(b) we show the patterns for $Ru_{2-x}Mn_{1+x}Al$ films with x = 0.1, 0.3, 0.5 and 0.6. The films are fully textured in the entire composition range, with only a minor secondary phase whose associated peaks are about 3 to 4 orders of magnitude less intense than the MRA peaks. A likely origin is a very small amount (< 1%) of either a Ru-Mn [29] or Ru-Al binary alloy in the film, or a Ru oxide at the interface between the film and the capping layer.

The RSM data was collected around the (113) reflection of MgO and shown in Fig. 2. The in-plane epitaxial relationship of MgO and MRA is assumed to be MgO [100] parallel MRA [110], therefore we label the MRA peak as the (204) reflection. We determined the in-plane (a) and out-of-plane lattice parameters (c). The epitaxy improves with increasing Ru content and the films are near-cubic, with a maximal tetragonal distortion $\left(\frac{c-a}{a}\right)$ of 1% found for $Ru_{1.6}Mn_{1.4}Al$. We summarise the structural parameters of the samples in Table 1. The degree of Ru order is estimated from the ratio $S = F_{002}^2/F_{004}^2$. $L2_1$-ordered ($Fm\bar{3}m$) $Ru_{2.0}Mn_{1.0}Al$ and $Ru_{1.0}Mn_{2.0}Al$ have S = 0.33 and 0.18, respectively. For the XA variants ($F\bar{4}3m$), both $Ru_{2.0}Mn_{1.0}Al$ (Ru on 4*b* and 4*d*, Mn in 4*c*) and $Ru_{1.0}Mn_{2.0}Al$ (Mn on 4*b* and 4*d*, Ru occupying 4*c*) have $S \approx$ 0.02. Complete disorder among all elements in all positions suppresses the (002) reflection completely and thus S = 0. We calculated the theoretical ratio S using the stoichiometries inferred from the densities

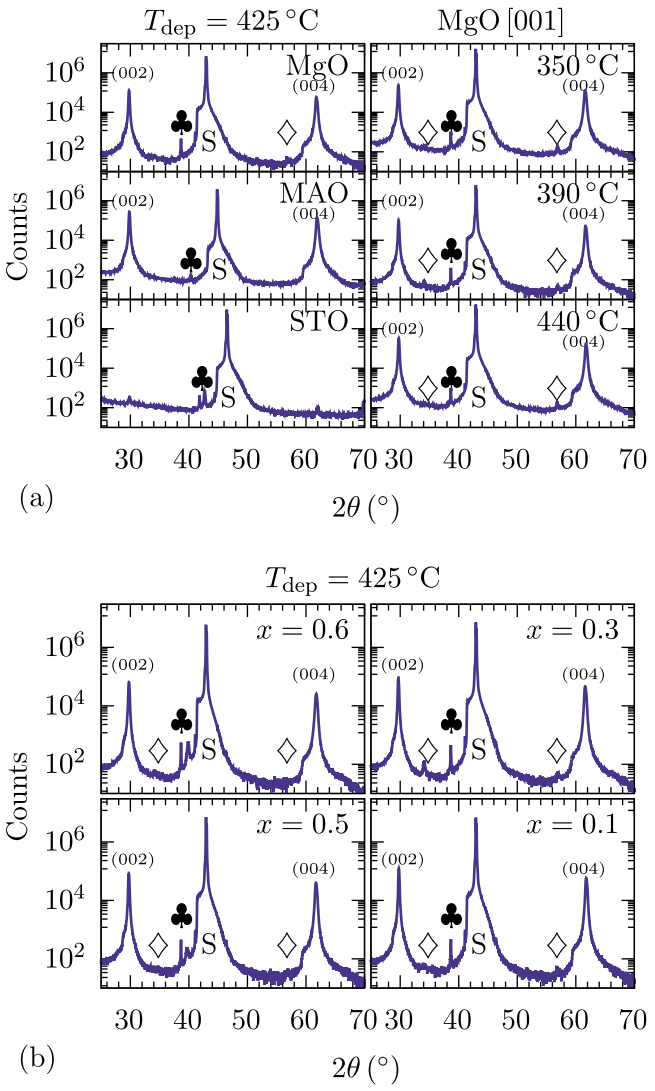

Fig. 1. X-ray diffraction patterns. (a) $Ru_{1.9}Mn_{1.1}Al$ deposited on MgO, MAO and STO substrates at $T_{dep} = 425\,°C$ (left column) and on MgO with varying T_{dep} (right column). (b) $Ru_{2-x}Mn_{1+x}Al$ deposited at $T_{dep} = 425\,°C$ for $x = 0.1$, 0.3, 0.5 and 0.6. The substrate (002) reflection is marked by 'S', while the corresponding Cu K_β reflection ($\lambda = 139.23$ pm) is marked by ♣. We also indicate a minor secondary phase (◇).

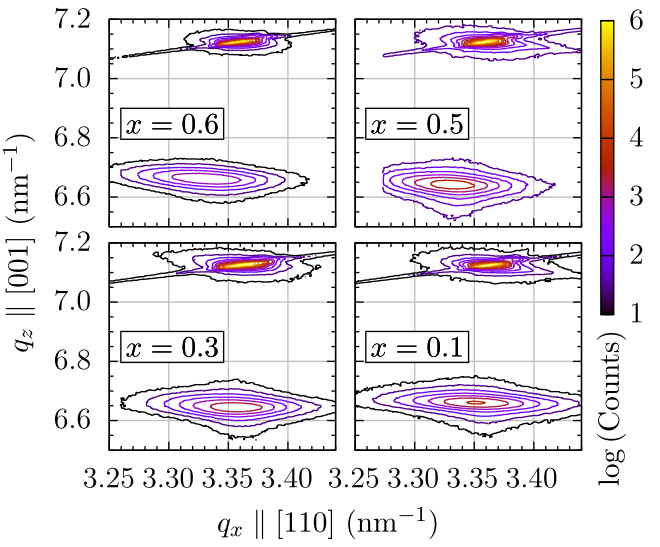

Fig. 2. Reciprocal space maps around the MgO [113] (MRA [204]) reflection from which we infer the in-plane lattice parameter of MRA. The MRA [100] direction is parallel to MgO [110].

Table 1
Crystal parameters of $Ru_{2-x}Mn_{1+x}Al$. The lattice parameters in columns three and four are determined from reciprocal space mapping, see Fig. 2. The experimentally observed ratio of $S = F^2_{002}/F^2_{004}$ is compared to that calculated for a fully ordered structure with the stoichiometry deduced from the film density. Mn fully occupies the 4*b* position, and Ru most of the 8*c*. The remaining 8*c* is filled by Mn. Al occupies only 4*a*.

#	x	a (pm)	c (pm)	S(exp)	S(th)
S08	0.10	596.80	600.53	0.25	0.26
S11	0.10	596.95	601.54	0.23	0.26
S13	0.10	597.17	600.79	0.23	0.26
S16	0.23	595.87	601.92	0.23	0.25
S12	0.25	596.05	602.31	0.20	0.25
S03	0.36	596.82	602.19	0.19	0.24
S09	0.49	600.81	602.12	0.24	0.23
S20	0.55	598	600	0.29	0.23
S15	0.61	600.41	600.39	0.30	0.22
S10	0.84	600.11	598.70	0.31	0.20

and an isotropic Debye–Waller factor of 0.3 Å^2 for all atoms. We find that for $x < 0.5$ the calculated and the observed S agree reasonably well, while for $x > 0.5$, the experimentally observed S is higher than predicted by the fully-ordered model indicating a degree of disorder. This disordered phase is likely to retain $Fm\bar{3}m$ symmetry, but with increased Debye–Waller factors. A much-improved agreement with the observed ratios for $x = 0.55$, 0.61 and 0.84 is obtained supposing the Debye–Waller factor is 0.9 Å^2.

3.2. Magnetism and magnetotransport properties

We now turn to the magnetotransport properties of MRA. In Fig. 3 we show magnetometry and anomalous Hall effect (AHE) loops of two representative samples, where the diamagnetic contribution from the substrate was subtracted as a linear slope in the magnetometry data, as was the high-field contribution to the transverse resistivity due to the normal Hall effect. The shape of the hysteresis loops recorded using the two techniques are near-identical suggesting that the AHE reflects the net magnetisation of the sample. Both magnetometry and AHE indicate weak easy-plane anisotropy, which is a result of the sample shape. A small contribution from perpendicular magnetocrystalline anisotropy due to the 1% tetragonal distortion of the unit cell is present and therefore $\mu_0 H_{an} < \mu_0 M_s$. We measured hysteresis loops of a $Ru_{1.9}Mn_{1.1}Al$ sample at different temperatures in order to extract M_s and H_{an}. From these we infer K_1 as a function of temperature. Assuming that $K_1(T) = K_1(0) \times \left(M_s(T)/M_0\right)^3$ we find $K_1(0) = 5.4$ kJ m^{-3}.

Weiss mean field theory was used to fit the temperature-dependent magnetisation data to obtain the exchange parameters and estimate the Curie temperature for $x = 0.10$. We take the Mn 4*b* moment to be 2.66 μ_B from the DFT calculation (see Fig. 7) giving a sublattice magnetisation of 451 kA m^{-1}. The Mn 8*c* (now 4*d*) is then deduced from the difference between the net magnetisation at low temperature and that of the Mn 4*b* and Ru 4*c* sublattices to be $\approx 3.1\ \mu_B$ per Mn or 92 kA m^{-1}. The choice of the quantum number S in the Brillouin function of the localised mean field theory is always problematic in a metal. It should somehow take account of the *d*-electron hybridisation with Al and Ru in our alloy. A choice of $S = 5/2$ for both Mn sites leads to an excellent fit of the experimental data with three molecular field coefficients n_{bb}, n_{bd} and n_{dd} and coordination numbers Z_{bb}, Z_{bd}, $Z_{dd} = 12$, 5.6, and 4.8 determined from the composition. Our fit indicates that the material orders just above room temperature at $T_C = 353$ K. Heisenberg exchange energies were calculated to be J_{bb}, J_{bd}, $J_{dd} = 0.96$, −2.40, and

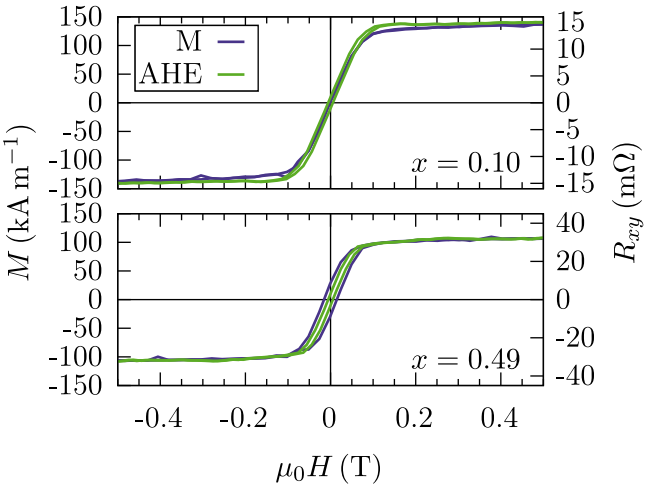

Fig. 3. Magnetometry and AHE recorded on two representative samples at 296 K. The applied magnetic field is perpendicular to the sample surface. In the upper panel, the AHE loop is plotted as a function of $(-\mu_0 H)$ for easier comparison with the magnetometry data. Both techniques indicate easy plane shape anisotropy with the saturation field (i.e. the anisotropy field) near-equal to $\mu_0 M_s$. The magnetometry data were corrected for the diamagnetism of the substrate by linear subtraction of the high field slope, as was the normal contribution to the transverse voltage.

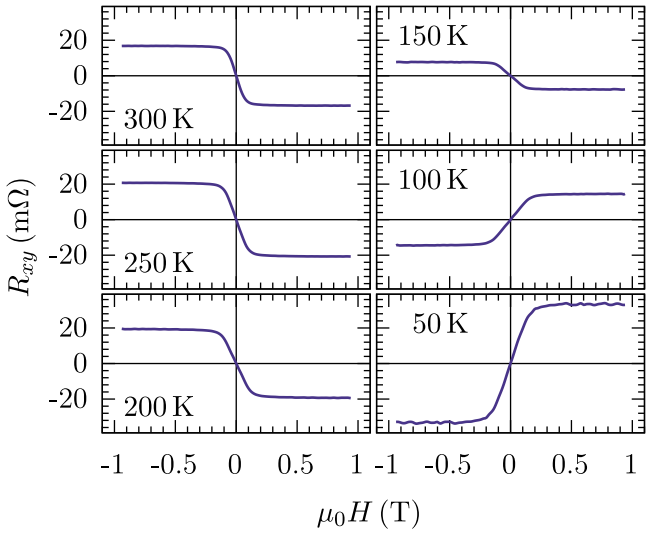

Fig. 4. AHE recorded at 300, 250, 200, 150, 100 and 50 K for sample S08. The sign of σ_{xy} changes between 150 K and 100 K, but the anisotropy field remains near constant, indicating that this change is due to a change in the nature (concentration and mobility) of the predominant charge carrier rather than crossing a temperature where magnetic compensation occurs.

Table 2
Summary of $Ru_{2-x}Mn_{1+x}Al$ magnetic and transport properties. The magnetisation decreases monotonically with increasing x for $x > 0.1$. We note that the sign of σ_{xy} changes at $x \approx 0.25$. In the approximation of a single species of carriers contributing to the transport, the carrier concentration n of the low-x samples ($x \lessapprox 0.25$) is approximately twice that of the high-x samples, while their mobility is half as great.

#	x	M_s (kA/m)	σ_{xx} (MS/m)	σ_{xy} (kS/m)	n (10^{28}/m^3)	μ (mV m/s^2)
S08	0.10	137	0.40	−0.71	3.69	0.06
S11	0.10	125	0.41	−0.81	2.18	0.10
S13	0.10	150	0.40	−0.62	2.03	0.10
S12	0.25	135	0.42	−1.38	2.76	0.08
S16	0.23	135	0.35	0.60	1.30	0.14
S03	0.36	130	n/a	n/a	n/a	n/a
S09	0.49	107	0.33	0.93	0.90	0.19
S20	0.55	100	n/a	n/a	n/a	n/a
S15	0.61	76	0.35	0.60	0.99	0.19
S10	0.84	25	n/a	n/a	n/a	n/a

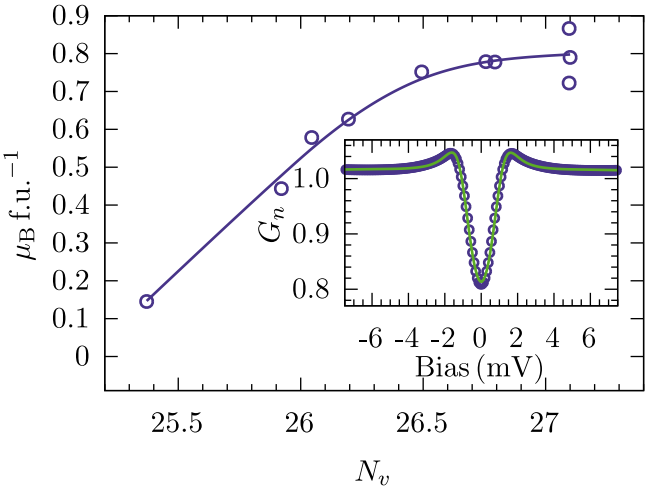

Fig. 5. Magnetisation of $Ru_{2-x}Mn_{1+x}Al$ as a function of number of valence electrons (N_v). The solid line is a guide to the eye. For $N_v \lessapprox 26.5$ the magnetisation increases by $\approx 0.6\ \mu_B$ f.u.$^{-1}$e^{-1}. The insert shows a point contact Andreev reflection (PCAR) spectrum for $x = 0.25$. The spin polarisation inferred from the fit (solid line) is $P = 52\,\%$.

1.33 meV per bond. The ratio of the product of the coordination number and the Heisenberg exchange energies is $J_{bb}Z_{bb} : J_{bd}Z_{bd} : J_{dd}Z_{dd}$ equal to $10 : -10 : 2.4$. The exchange is a factor of two smaller than for MRG, which explains the lower Curie temperature. The net anisotropy constant is smaller than for MRG reflecting the shared crystal structure and the similar degree of tetragonal distortion.

From the observed transverse (ρ_{xy}) and longitudinal (ρ_{xx}) resistivity we determine the carrier concentration and mobility assuming a single species of charge carriers. The results are summarised in Table 2. The magnetic ordering temperature is above room temperature for $x \lessapprox 0.6$.

The sign of the transverse conductivity $\sigma_{xy} \approx \rho_{xy}/\rho_{xx}^2$ changes at $x \approx 0.26$. Such a sign change is usually attributed to crossing the compensation point where $M_s \approx 0$. In Fig. 4 we plot the transverse resistance measured for $Ru_{1.9}Mn_{1.1}Al$ at 300, 250, 200, 150, 100 and 50 K. As when changing x, its sign changes between 150 K to 100 K. The anisotropy field, however, changes monotonically from 0.1 T to 0.2 T between room temperature and 50 K without any divergence indicating an M_s close to zero. We therefore attribute the sign change to a temperature-dependent filling of two or more pockets in the band structure near the Fermi energy, in agreement with the change of carrier concentration and their mobility shown in Table 2. The change in the anisotropy field due to shape anisotropy suggests the saturation magnetisation increases by $\approx 0.9\ \mu_B$f.u.$^{-1}$ between 300 K to 50 K, in agreement with low-temperature magnetometry measured on other samples (not shown).

The results indicate that $Ru_{2-x}Mn_{1+x}Al$ is a ferrimagnet where Ru in 8c and Mn in 4b form antiparallel ferromagnetic sublattices. No compensation composition is found in the range of x we have investigated, nor is there a compensation temperature due to the different local environments of Mn and Ru. Two (or more) species of charge carriers with opposite spin dominate the Fermi level, and their concentrations and mobilities differ by around a factor of two. $Ru_{2-x}Mn_{1+x}Al$ is not a half metal. In Fig. 5 we show the saturation magnetisation at 300 K as a function of the number of valence electrons N_v. The dependence is non-linear, however for low $N_v < 26.3$, the magnetisation increases with $0.6\ \mu_B$ f.u.$^{-1}$ e^{-1}, suggesting a spin polarisation P around 60 % in this region. The insert in Fig. 5 shows point-contact Andreev reflection

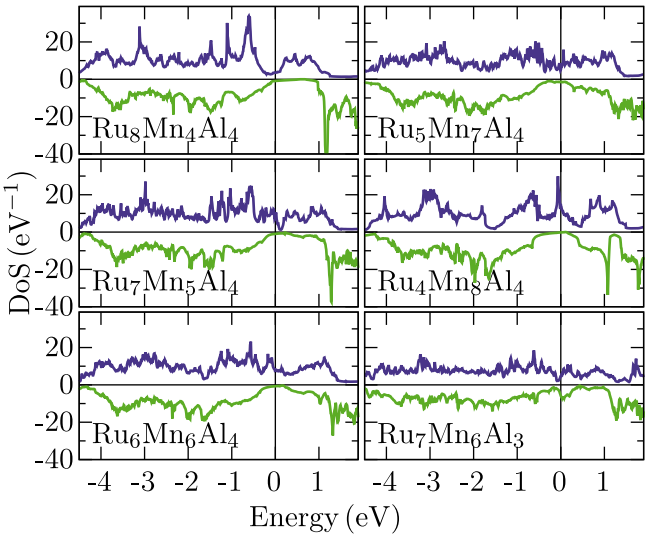

Fig. 6. Density of states for $Ru_{2-x}Mn_{1+x}Al$ with x ranging from 0 to 1. The composition $Ru_7Mn_6Al_3$ was selected as it corresponds closely to the experimental sample S16. It illustrates the change in the density of states due to the under stoichiometry in Al, although neither the spin polarisation ($P \approx 50\,\%$) nor the magnetic moment ($M \approx 1.5\ \mu_B$ f.u.$^{-1}$) changes significantly compared to the ordered version ($Ru_7Mn_5Al_4$).

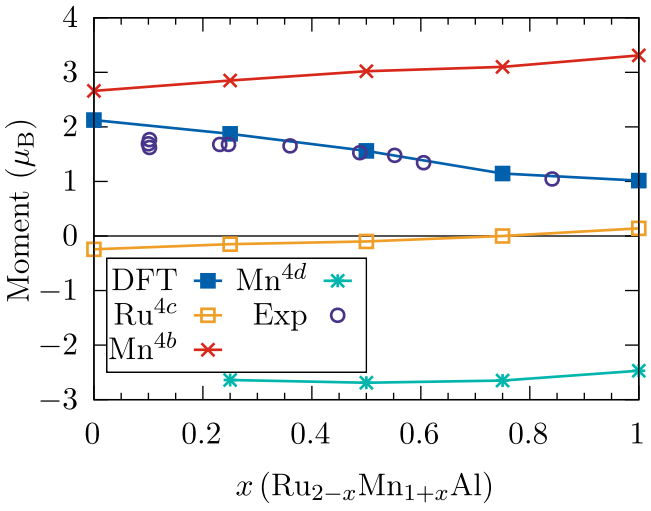

Fig. 7. Experimental and calculated net and sublattice moments for x in the range 0 to 1. The net calculated and experimental moments are given per formula unit. Note that the experimental values have been shifted by 0.9 μ_B f.u.$^{-1}$ to account for the higher magnetisation at $T = 0$ K.

recorded on $Ru_{1.6}Mn_{1.4}Al$. We find the spin polarisation $P = 52\,\%$ in good agreement with that inferred from the plot of M against N_v.

3.3. Comparison with density functional theory

Finally we compare our results with *ab initio* calculated magnetisation and density of states. We used a 16-atom cell for all our calculations, and relaxed both lattice parameters (a and $c \approx 600$ pm) and magnetic moments, but kept the individual atoms at their assigned Wychoff positions in agreement with the structural model inferred from the analysis of the X-ray data above. For all compositions investigated, the lattice parameters relax to cubic symmetry ($a = b = c$). In Fig. 6 we show the density of states (DoS) around the Fermi level for a series of $Ru_{2-x}Mn_{1+x}Al$ samples with varying x. The label on each panel corresponds to the content of the 16-atom cell used for calculations, with Ru occupying the 8c and Mn and Al the 4b and 4a positions, respectively. For $Ru_{2.0}Mn_{1.0}Al$, in particular, there is a gap in the spin down DoS, but its onset is almost 1 eV above the Fermi level. With decreasing Ru (and increasing Mn) the gap moves closer towards the Fermi level, but is simultaneously destroyed by the creation of supplementary states in the gap. None of the compositions are half metallic, although perfectly ordered $Ru_{1.0}Mn_{2.0}Al$ in the middle right panel of Fig. 6 comes close. We have seen above that this composition disorders during growth. The bottom right panel of Fig. 6 illustrates the effect of Al substoichiometry. From these figures we estimate the spin polarisation of MRA to be around 50 %, in good agreement with the experimental results.

We also show, in Fig. 7, the site- and ion-resolved magnetic moments obtained by theory. The net magnetisation decreases from $\approx 2\ \mu_B$ f.u.$^{-1}$ to 1 μ_B f.u.$^{-1}$ for x in the range 0 to 1. Mn in the 4b position carries a strong moment $\approx 3\ \mu_B$ that increases with increasing x, suggesting increased localisation of the 3d bands. As x is raised above zero, some Mn fills the 8c (now 4d) position and it is coupled antiferromagnetically to Mn in 4b, but ferromagnetically to the remaining Ru (in 8c/4c). Ru carries a small moment in all compositions, but interestingly changes sign at $x \approx 0.75$. In the figure we also plot the experimentally observed magnetisation, offset by 0.9 μ_B f.u.$^{-1}$ to account for the decrease of the magnetisation between $T = 0$ K and 300 K (see above).

4. Conclusions

We find that $Ru_{2-x}Mn_{1+x}Al$ crystallises on MgO and $MgAl_2O_4$ with a slight substrate-induced tetragonal distortion of the cubic $Fm\bar{3}m$ crystal structure. For low values of x (<0.5), the structure remains essentially ordered with Ru in the 8c position and Mn and Al in 4b and 4a, respectively, with the additional Mn filling the sites vacated by Ru. As x is increased further, the crystal structure evolves towards $F\bar{4}3m$, although order between the 4c and 4d sites does not occur, and additionally at low x, the 4a – 4b order is perturbed. All compositions are magnetically ordered and exhibit a high spin polarisation of around 50%. *Ab initio* calculations agree well with the observed crystal structure and magnetic mode. MRA is ferrimagnetic, with Mn in the 4b position coupling antiferromagnetically to Ru in 8c. Two or more species of charge carriers close to or at the Fermi level account for the reduction of the spin polarisation and the change in the sign of the Hall conductivity with x and T. In contrast to MRG, where the spin polarisation as inferred from the Slater-Pauling plot [17] is close to $P = 100\%$, the anomalous Hall angle (σ_{xy}/σ_{xx}) of MRA is only ~2‰, more than an order of magnitude less than for MRG despite a higher concentration of Ru.

When x is increased above ≈ 0.6, MRA no longer exhibits AHE at room temperature although the crystal structure is increasingly similar to that of MRG, albeit with a higher atomic concentration of Ru. MRG exhibits the strongest spin–orbit-related effects when there are less than half a Ru per formula unit on average. We therefore conclude that Ga, and not Ru, is promoting high conduction band spin orbit coupling in MRG, and helps to move the Fermi level into the spin gap by allowing Ga-Mn antisites to form [30]. The analysis of the X-ray diffraction diagrams above (Table 1) suggests that MRA is best described by space group $Fm\bar{3}m$ ($L2_1$) for all values of x. Mn replacing Ru in the 8c positions does not order and the crystal structure remains centrosymmetric. MRG crystallises in space group $F\bar{4}3m$ (XA) as the 8c position in $Fm\bar{3}m$ is occupied by ordered Ru and Mn on 4d and 4c in $F\bar{4}3m$. It has no centre of inversion. For MRG, a topological contribution to the transverse conductivity is allowed by symmetry.

At $x = 0$, the Mn-Mn distance is 600 pm, and the Mn orders ferromagnetically. The moment carried by Ru is small, and it is unlikely that the magnetic order is due to the Ru-Mn AFM interaction. The question of the nature of this long-distance exchange interaction arises. Several other Heusler alloys (Rh_2Mn(Pb;Sn;Ge) and Cu_2Mn(In;Sn;Al)) [31,32]

where only one out of four atoms per formula is manganese order ferromagnetically above 300 K, and Au_4Mn [33] with a shorter first neighbour Mn-Mn distance of 404 pm has a Curie point at 390 K. There, all the exchange interactions up to the tenth nearest-neighbours at 1000 pm are either ferromagnetic or zero. Since different elements are present in these dilute Mn-based ferromagnets, it is likely that long-range ferromagnetic exchange is mediated by a *p*-band. The Mn-Mn exchange (in Au_4Mn) only becomes oscillatory and RKKY-like at Mn-Mn distances exceeding 1040 pm.

In summary, $Ru_{2-x}Mn_{1+x}Al$ is a ferrimagnetic Heusler alloy with high spin polarisation and magnetic ordering at room temperature. The absence of signifiant spin–orbit coupling precludes perpendicular magnetic anisotropy as well as any notable magneto-resistive effects. This contrast with MRG where Al is replaced by Ga, is likely due to a combination of two effects. First, the hybridisation of the Mn $3d$ and $3s$ states with $3p$ bands of Al as opposed to the $4p$ bands of Ga. Second, for the MRG XA ($F\bar{4}3m$) crystal structure, the noncentrosymmetric character of the Mn sublattices contributes to intrinsic AHE and a large Hall angle. The $L2_1$ ($Fm\bar{3}m$) structure of MRA is centrosymmetric.

CRediT authorship contribution statement

K.E. Siewierska: Validation, Investigation, Writing – original draft, Visualization. **H. Kurt:** Conceptualization, Methodology, Investigation. **B. Shortall:** Investigation. **A. Jha:** Investigation. **N. Teichert:** Investigation. **G. Atcheson:** Investigation. **M. Venkatesan:** Investigation. **J.M.D. Coey:** Conceptualization, Writing – review & editing, Supervision, Funding acquisition. **Z. Gercsi:** Methodology, Validation, Investigation, Visualization, Formal analysis. **K. Rode:** Conceptualization, Methodology, Validation, Formal analysis, Writing – review & editing, Visualization, Supervision.

Declaration of competing interest

The authors declare that they have no known competing financial interests or personal relationships that could have appeared to influence the work reported in this paper.

Data availability

Data will be made available on request.

Acknowledgements

K.E.S. and J.M.D.C. acknowledge funding through Irish Research Council, Ireland under Grant GOIPG /2016/308 and in part by the Science Foundation Ireland under Grants 12/RC/2278 and 16/IA/4534. B.S. acknowledges funding from the Irish Research Council, Ireland Grant EPSPG/2020/106G.A. A.J., G.A., Z.G., and K.R. acknowledge funding from 'TRANSPIRE' FET Open Programme, H2020. N.T. was supported by the European Union's Horizon 2020 Research and Innovation Programme under Marie Skłodowska-Curie EDGE Grant 713567. H.K. and M.V. were funded through the 'ZEMS' contract, Science Foundation Ireland, grant 16/IA/4534.

References

[1] L. Wollmann, A.K. Nayak, S.S. Parkin, C. Felser, Annu. Rev. Mater. Res. 47 (1) (2017) 247–270.
[2] T. Graf, C. Felser, S.S. Parkin, Prog. Solid State Ch. 39 (1) (2011) 1–50.
[3] N. Teichert, G. Atcheson, K. Siewierska, M.N. Sanz-Ortiz, M. Venkatesan, K. Rode, S. Felton, P. Stamenov, J.M.D. Coey, Phys. Rev. Mater. 5 (2021) 034408.
[4] K.E. Siewierska, N. Teichert, R. Schäfer, J.M.D. Coey, IEEE Trans. Magn. 55 (2) (2019) 1–4.
[5] C. Banerjee, N. Teichert, K. Siewierska, Z. Gercsi, G. Atcheson, P. Stamenov, K. Rode, J.M.D. Coey, J. Besbas, Nature Commun. 11 (2020) 4444.
[6] N. Thiyagarajah, Y.-C. Lau, D. Betto, K. Borisov, J.M.D. Coey, P. Stamenov, K. Rode, Appl. Phys. Lett. 106 (12) (2015) 122402.
[7] K. Borisov, D. Betto, Y.C. Lau, C. Fowley, A. Titova, N. Thiyagarajah, G. Atcheson, J. Lindner, A.M. Deac, J.M.D. Coey, P. Stamenov, K. Rode, Appl. Phys. Lett. 108 (19) (2016) 192407.
[8] H. van Leuken, R.A. de Groot, Phys. Rev. Lett. 74 (7) (1995) 1171–1173.
[9] I. Galanakis, P. Mavropoulos, P. Dederichs, J. Phys. D Appl. Phys. 39 (5) (2006) 765.
[10] S. Wurmehl, H.C. Kandpal, G.H. Fecher, C. Felser, J. Phys.: Condens. Matter 18 (27) (2006) 6171.
[11] M.E. Jamer, Y.J. Wang, G.M. Stephen, I.J. McDonald, A.J. Grutter, G.E. Sterbinsky, D.A. Arena, J.A. Borchers, B.J. Kirby, L.H. Lewis, B. Barbiellini, A. Bansil, D. Heiman, Phys. Rev. Appl. 7 (2017) 064036.
[12] H.-W. Bang, W. Yoo, C. Kim, S. Lee, J. Gu, Y. Park, K. Lee, M.-H. Jung, Appl. Phys. Lett. 115 (1) (2019) 012402.
[13] H. Kurt, K. Rode, M. Venkatesan, P. Stamenov, J.M.D. Coey, Phys. Status Solidi b 248 (10) (2011) 2338–2344, http://dx.doi.org/10.1002/pssb.201147122.
[14] R. Zhang, Z. Gercsi, M. Venkatesan, A. Jha, P. Stamenov, J. Coey, J. Magn. Magn. Mater. 501 (2020) 166429.
[15] X. Liu, I. Ohnuma, R. Kainuma, K. Ishida, J. Phase Equilib. 20 (45) (1999) 45–56.
[16] H. Kurt, K. Rode, P. Stamenov, M. Venkatesan, Y.-C. Lau, E. Fonda, J.M.D. Coey, Phys. Rev. Lett. 112 (2014) 027201.
[17] K.E. Siewierska, G. Atcheson, A. Jha, K. Esien, R. Smith, S. Lenne, N. Teichert, J. O'Brien, J.M.D. Coey, P. Stamenov, K. Rode, Phys. Rev. B 104 (2021) 064414.
[18] R. Stinshoff, G.H. Fecher, S. Chadov, A.K. Nayak, B. Balke, S. Ouardi, T. Nakamura, C. Felser, AIP Adv. 7 (10) (2017) 105009.
[19] R. Stinshoff, A.K. Nayak, G.H. Fecher, B. Balke, S. Ouardi, Y. Skourski, T. Nakamura, C. Felser, Phys. Rev. B 95 (2017) 060410.
[20] J. Finley, C.-H. Lee, P.Y. Huang, L. Liu, Adv. Mater. (Deerfield Beach, Fla.) 31 (2) (2019) e1805361.
[21] J. Finley, L. Liu, Appl. Phys. Lett. 116 (11) (2020) 110501.
[22] C. Banerjee, K. Rode, G. Atcheson, S. Lenne, P. Stamenov, J.M.D. Coey, J. Besbas, Phys. Rev. Lett. 126 (2021) 177202.
[23] C.S. Davies, G. Bonfiglio, K. Rode, J. Besbas, C. Banerjee, P. Stamenov, J.M.D. Coey, A.V. Kimel, A. Kirilyuk, Phys. Rev. Res. 2 (2020) 032044.
[24] D. Betto, K. Rode, N. Thiyagarajah, Y.-C. Lau, K. Borisov, G. Atcheson, M. Žic, T. Archer, P. Stamenov, J.M.D. Coey, AIP Adv. 6 (5) (2016) 055601.
[25] M. Chen, R. Mishra, Y. Wu, K. Lee, H. Yang, Adv. Opt. Mater. 6 (17) (2018) 1800430.
[26] P. Stamenov, J. Appl. Phys. 113 (17) (2013) 17C718.
[27] K. Borisov, C.-Z. Chang, J.S. Moodera, P. Stamenov, Phys. Rev. B 94 (2016) 094415.
[28] OpenMX Website.
[29] M. Yin, P. Nash, J. Alloys Compd. 634 (2015) 70–74.
[30] M. Žic, K. Rode, N. Thiyagarajah, Y.-C. Lau, D. Betto, J.M.D. Coey, S. Sanvito, K.J. O'Shea, C.A. Ferguson, D.A. MacLaren, T. Archer, Phys. Rev. B 93 (2016) 140202(R).
[31] H.P.J. Wijn, in: H.P.J. Wijn (Ed.), Magnetic Properties of Metals: D-Elements, Alloys and Compounds, in: Data in Science and Technology, Springer Berlin, Heidelberg, 1991.
[32] J.C. Suits, Phys. Rev. B 14 (1976) 4131–4135.
[33] Y. He, Z. Gercsi, R. Zhang, Y. Kang, Y. Skourski, L. Prendeville, O. Larmour, J. Besbas, C. Felser, P. Stamenov, J.M.D. Coey, Phys. Rev. B 106 (2022) 214414.